



## ORIGINAL ARTICLE

# Extraction and characterization of highly pure alumina ( $\alpha$ , $\gamma$ , and $\theta$ ) polymorphs from waste beverage cans: A viable waste management approach



Md. Lutfor Rahman<sup>a,\*</sup>, Md. Sydul Islam<sup>b</sup>, Md. Farid Ahmed<sup>a</sup>, Bristy Biswas<sup>a</sup>, Nahid Sharmin<sup>a</sup>, A J M Tahuran Neger<sup>a</sup>

<sup>a</sup> Institute of Glass and Ceramic Research and Testing (IGCRT), Bangladesh Council of Scientific and Industrial Research (BCSIR), Dhaka-1205, Bangladesh

<sup>b</sup> Department of Applied Chemistry and Chemical Engineering, Noakhali Science and Technology University, Noakhali-3814, Bangladesh

Received 16 September 2022; accepted 8 December 2022

Available online 14 December 2022

## KEYWORDS

Waste beverage cans;  
Precipitation method;  
( $\gamma$ ,  $\theta$ ,  $\alpha$ )-alumina polymorphs;  
XRD;  
SEM;  
Optical property

**Abstract** The recycling and recovery of important materials from inexpensive feedstock has now become an intriguing area and vital from commercial and environmental viewpoints. In the present work, extraction of different single phases of alumina ( $\alpha$ ,  $\gamma$ ,  $\theta$ -Al<sub>2</sub>O<sub>3</sub>) having high purity (> 99.5 %) from locally available waste beverage cans (~95 % Al) through facile precipitation route calcined at distinct temperatures has been reported. The optimization of process technology was done by a variety of different synthesis parameters, and the production cost was estimated between 84.47–87.45 USD per kg of alumina powder. The as prepared alumina fine particles have been characterized using different sophisticated techniques viz. TG-DTA, WD-XRF, XRD, FT-IR, SEM, DLS-based particle size analysis (PSA) with zeta ( $\zeta$ ) potential measurement and UV–Visible Spectroscopy. X-ray diffractogram confirms the formation of  $\gamma$ -,  $\theta$ -, and  $\alpha$ -alumina at 500–700 °C, 900–1000 °C, and 1200 °C respectively and crystallite size, crystallinity, strain, dislocation density, and specific surface area were measured using major X-ray diffraction peaks which varies with temperature. The SEM studies showed that the as prepared alumina particles were agglomerated, irregular-shaped with particle size (0.23–0.38  $\mu$ m), pore size, and porosity were calculated from SEM image.  $\zeta$ -potentials at different pH values as well as isoelectric point (IEP) of  $\alpha$ ,  $\gamma$ , and  $\theta$  alu-

\* Corresponding author.

E-mail addresses: lutforrahman@bcsir.gov.bd, lutforju33@yahoo.com, lutforju33@gmail.com (M.L. Rahman).

Peer review under responsibility of King Saud University.



mina were calculated in an aqueous medium which changes with temperature. The direct band gap ( $E_g$ ) energies were found between 4.09 and 5.19 eV of alumina obtained from different calcination temperatures. The synthesized materials can be used in sensors, ceramics, catalysis, and insulation applications.

© 2022 The Author(s). Published by Elsevier B.V. on behalf of King Saud University. This is an open access article under the CC BY-NC-ND license (<http://creativecommons.org/licenses/by-nc-nd/4.0/>).

## 1. Introduction

In the era of today's swift industrialization and urbanization, the development of industrial wastes is escalating unfortunately which eventually exacerbates the environmental and socioeconomic problems. Aluminum (Al) cans, owing to the excellent food quality preservation advantages, are one of the most widely utilized goods in the food and beverages packaging industry (Marsh and Bugusu, 2007). The global Al cans market is forecasted to extend up to \$55.31 billion by 2026, showing a 4.29 % growth between 2021 and 2026 (ReportLinker, 2021). Globally, people are consuming soda and beer in millions of beverage cans every day that reaching to  $2 \times 10^{11}$  cans per year and subsequently generating ca.  $6 \times 10^9$  kg of waste every year. Moreover, ca. 1 % of the anthropogenic greenhouse gas (GHG) originates from the Al industry at the present time. However, since waste beverage cans (WBCs) contain mostly aluminum (> 90 %), these can be utilized by recycling into different beneficial products. Besides, from the environmental perspective, reusing and recycling of WBC is favorable due to the conservation of resources, energy savings as well as avoidance of littering (Council, 1999; El-Amir et al., 2016; Osman et al., 2017; Risonarta et al., 2019; Sercombe, 2010).

In recent years research and advancement aluminum oxide ( $Al_2O_3$ ) or alumina become a significant material and widely attracted the scientific communities' interest owing to its flabbergasting physicochemical properties, such as high thermodynamic stability high hardness, great dielectric strength, extreme chemical resistance, transparency, and comparatively high electrical conductivity for ceramic materials, etc (Busca, 2014; Huang et al., 2008). Due to these distinct properties, alumina has plenty of industrial and technological uses, for example,  $\alpha$ - $Al_2O_3$  is used in advanced ceramics, microelectronic packaging, catalysis, and coating (Chen et al., 2014; Lafficher et al., 2017; Roslyakov et al., 2017; Touzin et al., 2010; Wang et al., 2021);  $\gamma$ - $Al_2O_3$  has high promising application as a catalyst/catalyst support, moisture sensor, and adsorbent material (Osman et al., 2017; Saha et al., 2016; Zabeti et al., 2009; Zhu et al., 2002);  $\theta$ - $Al_2O_3$  can be potentially exploited in the fast optical sensor ( $\sim 2.23$  ns decay time), catalysis as a metal catalyst support and dielectronic fields (Busca, 2014; Gangwar et al., 2014; Huang et al., 2008; Hurtado et al., 2004).

Alumina can exist in different structural polymorphs that are stable over a broad range of temperatures. Alpha alumina ( $\alpha$ - $Al_2O_3$ ), popularly known as corundum, is the most stable phase, which typically occurs at high temperatures following a set of polymorphic transformations, while other metastable transition aluminas, viz.,  $\gamma$ - $Al_2O_3$ ,  $\delta$ - $Al_2O_3$ , and  $\theta$ - $Al_2O_3$ , etc. are formed at lower temperatures during the heat treatment (Hakkar et al., 2019; Levin and Brandon, 1998; Matori et al., 2012). The sequence can be shown as the dehydroxylation of  $Al(OH)_3$  (Bayerite) as follows (Temuujin et al., 2000):  $Al(OH)_3 \rightarrow$  Transition aluminas  $\rightarrow \alpha$ - $Al_2O_3$ .

Alumina powders can be prepared by different routes such as mechanical milling, hydrothermal, combustion, thermal plasma, vapor deposition, sol-gel, laser ablation method, etc. Many of these techniques require specialized equipment, toxic organic compounds, expensive chemicals, have the particle with extremely low specific surface area, low yield and purity, emit noxious gases (Ananthapadmanabhan et al., 2004; El-Amir et al., 2016; Ghanizadeh et al., 2014; Ibrahim and Abu-Ayana, 2008a; Jolly and Bhattacharya, 2018; Kelekanjeri et al., 2006; Piriawong et al., 2012; Suchanek, 2010; Suryanarayana, 2005; Tok et al., 2006; Wu, 2001).

The aqueous precipitation method has appeared to be a facile, economical, safe, and has a short cycle chemical path which can be employed for a rapid production process for generating highly pure alumina with excellent yield (Du et al., 2009; El-Amir et al., 2016; Feng et al., 2017; Theiss et al., 2016). There was an attempt from Chotisuwan *et al.* to prepare alumina from discarded Al cans via a sol-gel approach, however, they used expensive mercury iodide and 2-propanol chemicals in the preparation (Chotisuwan et al., 2012). Matori and coworkers synthesized  $\alpha$ - $Al_2O_3$  with 96 % purity from waste cans via precipitation method using sulphuric acid as leachant and ethanol as precipitant, however, they got 96.78 % product purity at 1400 °C calcination temperature and no single-phase theta or gamma alumina were observed. They found mixed alumina phases ( $\gamma$ ,  $\theta$ ,  $\delta$ ) at and after the calcination at 900 °C (Matori et al., 2012). In addition, no systematic studies have been reported on the influence of reaction time, alkali chemical agent, and pH value of the precipitating agent in the preparation of alumina particles from WBCs.

Accordingly, in this study, we report the effective recycling of waste beverage cans by using it as a raw material to synthesize valuable alumina polymorphs via precipitation method using hydrochloric acid as leachant and precipitant along with alkali treatment of sodium hydroxide to form soluble aluminate and separate impurities. To the best of our knowledge, no alike case has yet been presented. This work was mainly attempted to alleviate the waste disposal issue and expand a facile and cost-effective synthetic route for producing potential alumina particles at optimal process conditions and examine their traits by using TG-DTA, WD-XRF, XRD, FT-IR, SEM, DLS based Particle size analysis (PSA) with Zeta potential and UV-vis. analyzes. The major aspect of this investigation is the endowing of an environmentally viable solution for the utilization of WBCs resources by means of a simplistic approach to beneficial materials.

## 2. Experimental

### 2.1. Materials

Discarded aluminum beverage cans of different brands were used as target waste raw material to prepare alumina powders, which were collected from the vicinity of local retail stores. The cans were heated slowly to remove the organic layer from the surface prior to the experiment which may impede reactants' contact. Analytical grade reagents such as hydrochloric acid (HCl, assay: 37 %) and sodium hydroxide pellets (NaOH, assay:  $\geq 99$  %) were bought from the local market and used without further purification. The NaOH solution (10 %) was prepared with a strength of 2.5 M in a volumetric flask. Deionized water (Type-II DI water, resistivity ca. 15.0 M $\Omega$ -cm) was used throughout the research work.

### 2.2. Synthesis of alumina ( $Al_2O_3$ ) from waste beverage cans (WBC)

Firstly, the aluminum cans body portion was cut into small sheets of 0.8 cm  $\times$  1.5 cm to increase the available surface area for a faster reaction with acid. We have simply used hand cut

technique to make small sheets of the waste aluminium beverage cans for laboratory scale. Subsequently, a weighted 5 g of can sheets were slowly treated with a leaching agent (30.0 ml of 1:1 HCl), to avoid any peril originating from the generated  $H_2$  in a 250 ml two-neck flat bottom flask with a water condenser. The mixture was then refluxed at 120 °C for 35 min under constant magnetic stirring to dissolve all the metals into solution. The reaction mixture was filtered in order to eliminate undissolved substances. The dropwise addition of an excess amount of sodium hydroxide (250 ml of 2.5 M NaOH solution) with stirring to the filtrate was then converted all the aluminum as soluble sodium aluminate ( $NaAlO_2$ ) and also promoted the separation of other insoluble fractions of impurities such as  $Fe(OH)_3$ ,  $Mg(OH)_2$ ,  $Mn(OH)_2$ , etc. Through filtration, the residue was separated and the existence of excess NaOH in the filtrate solution was neutralized by adding 70 ml of HCl (1:1) and a white precipitate of aluminum hydroxide was formed at once. The obtained  $Al(OH)_3$  was centrifuged and repeatedly washed with deionized water to remove unwanted ions like  $Na^+$ ,  $Cl^-$ , followed by oven-drying at 110 °C for 12 h to remove the residual amount of moisture. Finally, the prepared dried powder was ground and calcined in a muffle furnace at different temperatures (280–1200 °C) under an air atmosphere for 4 h with the temperature steps of 5 °C  $min^{-1}$  to obtain alumina ( $Al_2O_3$ ) powders.

The flowchart of the of  $Al_2O_3$  preparation from WBC waste sources is shown in Fig. 1.

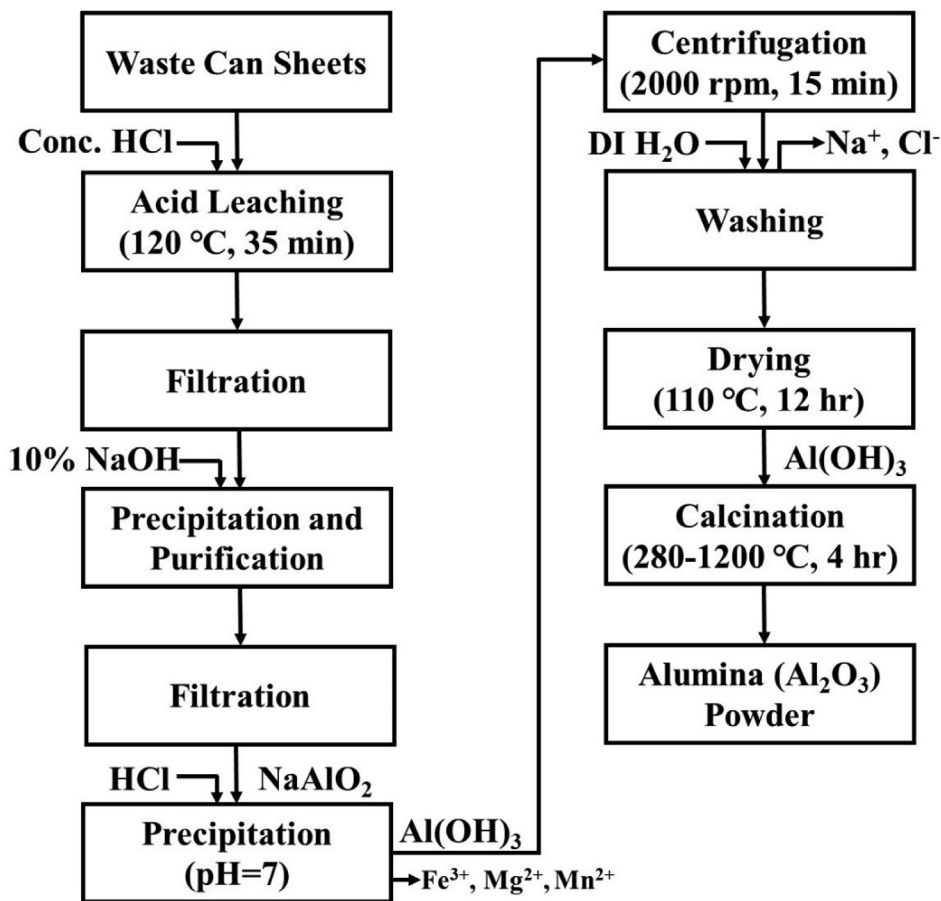
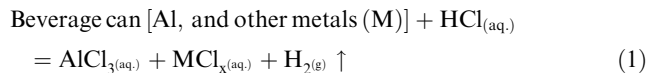
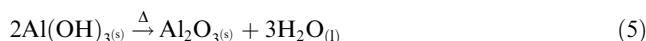
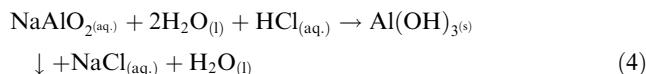
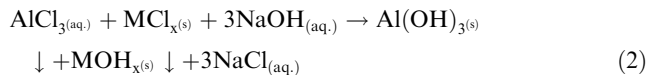


Fig. 1 Flowchart of alumina powders production from WBC waste.

### 2.3. Reactions



(where  $x$  is a positive integer)



### 2.4. Characterization

The thermal traits of the intermediate  $Al(OH)_3$  sample were evaluated with a combined EXSTAR 6300 TG-DTA thermal analyzer (Seiko Instruments Inc., Japan) at a scan rate of 20 °C/min under  $N_2$  atmosphere heating from 25 °C to 1020 °C. The crystallographic characteristics of the alumina

samples were recorded on a Phillips X'Pert Pro X-ray Diffractometer (PANalytical Pro PW 3040, Netherlands) using Ni filter and monochromatic  $\text{CuK}\alpha$  ( $K\alpha = 1.5406 \text{ \AA}$ ) radiation between  $20^\circ$  to  $80^\circ$  generated at 40KV and 30 mA with scanning speed 4.01/min ( $0.02^\circ/2\theta$  step). The X-ray diffraction (XRD) patterns were probed, and possible peaks were spotted by comparing them with the International Centre for Diffraction Data (ICDD) database. For chemical compositional analysis of raw materials and products, a Rigaku Wavelength-Dispersive X-ray Fluorescence (WD-XRF) Spectrometer (ZSX Primus IV, Japan) incorporated with an Rh target X-ray tube was employed. The Fourier Transform Infrared Spectroscopy (FTIR) spectra were recorded on a PerkinElmer FT-IR spectrophotometer integrated with diamond attenuated total reflection (Frontier, UK) between 4000 and  $400 \text{ cm}^{-1}$  region. The measurements of pH were carried out by a Hanna pH/mV Meter (HI2211-01, USA) equipped with a HI1131B pH electrode. To measure both the mean size of particles at neutral pH and surface charge distribution ( $\zeta$ -potential) for pH values between 5 and 11 of the prepared samples, Nanopartica Analyzer (SZ-100, HORIBA Scientific, Japan) instrument was used. The sample preparation for determining  $\zeta$ -potentials was done by suspending 10 mg of  $\text{Al}_2\text{O}_3$  sample in 100 ml DI water followed by 1 hr sonication in an ultrasonic bath. After settling of suspension, the samples were loaded into a 1 cm cuvette for the measurement. The adjustment of suspensions pH values was done by adding HCl and ammonia solutions. The UV-vis absorption spectra of prepared samples suspended in DI water were taken using a Hitachi UV-vis Spectrophotometer (UH5300, Japan) between 200 and 900 nm wavelength region. The morphological investigations of prepared  $\text{Al}_2\text{O}_3$  samples were done with a Zeiss Evo® Scanning Electron Microscope (MA15 VP-SEM, UK) operated at 10 kV.

### 3. Results and discussion

#### 3.1. Compositional analysis and product cost estimation

The compositional analysis report by WDXRF of both the target raw materials (i.e., WBC of different brands) and extracted  $\text{Al}_2\text{O}_3$  powder after calcination is tabulated in Table 1. A detailed analysis report of all brand waste beverage cans is listed in Table S1. The analysis revealed that there is a high proportion of aluminum content ( $\sim 94.63 \%$ ) in raw material shaping it a potential candidate for the extraction of  $\text{Al}_2\text{O}_3$  from WBC. The other associated elements such as manganese,

iron, magnesium, copper, zinc, etc. found pretty much in a lower amount. In the case of alumina products, it mainly consists of  $\text{Al}_2\text{O}_3$  ( $\sim 99.51 \%$ ) with a minute quantity of other oxide contents, demonstrating a high level of purity of the extracted alumina powder. This high-grade alumina can be an ideal option for different engineering and technological applications.

The approximate production cost of waste beverage cans (WBC) derived alumina powder per kg via precipitation extraction method is listed in Table 2. The approximate expense of synthesized alumina powders ( $\sim 0.29 \mu\text{m}$  average sized  $\text{Al}_2\text{O}_3$  particles) is ranged between 84.47 and 87.45 USD per kg. Subsequently, the commercially available  $\text{Al}_2\text{O}_3$  powdered market price is between 140 and 7000 USD per kg, relying on the purity level, specific surface area, application grade, and size of the alumina particle (Alfa Aesar, 2022; Fisher-Scientific, 2022; MIC, 2022; MSE Supplies, 2022; Sigma-Aldrich, 2022a, 2022b, 2022c). It is concluded that the (WBC) derived highly pure (99.51 %)  $\text{Al}_2\text{O}_3$  powders through the precipitation extraction approach are eco-benign and economically viable in comparison to existing available aspects. Besides, if the generated  $\text{H}_2$  gas during the extraction process (Eq. (1)) is collected and deposited, it can also be exploited as a source of fuel (Adans et al., 2016; Durbin and Malardier-Jugroot, 2013; Dutta, 2014).

#### 3.2. Optimization of reaction parameters on $\text{Al}_2\text{O}_3$ yield

To evaluate the effects of different variable parameters on  $\text{Al}_2\text{O}_3$  particles synthesis, three sets of experiments were conducted where one parameter's value (either reaction time or NaOH or HCl) was altered at a time. Optimizing these conditions leads to having a better yield of  $\text{Al}_2\text{O}_3$  with less expense and effective utilization of WBC sources while minimizing the impurities amount to a feasible extent.

#### 3.3. Effect of reaction time

The influence of the reaction time on the extent of the yield of  $\text{Al}_2\text{O}_3$  products is shown in Fig. 2(a). Here, six experiments were conducted where the variation of reaction time lengths of 20, 25, 30, 35, 40, and 50 mins was investigated during refluxing of the mixture at  $120^\circ\text{C}$  under stirring. After completion of the reaction, all other steps in the process were corresponding to those narrated in the experimental section. It is quite clear that the percentage of yield raised gradually with increasing time from 20 to 50 mins for reaction. Although

**Table 1** Chemical composition of WBC raw material and  $\text{Al}_2\text{O}_3$  powder product analyzed by WDXRF.

| Raw Material Analysis |                       |       |                         |                |       |                      |      |       |                         |      |       |      |        |
|-----------------------|-----------------------|-------|-------------------------|----------------|-------|----------------------|------|-------|-------------------------|------|-------|------|--------|
| Analyte               | Mg                    | Al    | Si                      | P              | S     | Cl                   | Cr   | Mn    | Fe                      | Ni   | Cu    | Zn   | Others |
| Composition (%)       | 0.69                  | 94.63 | 0.36                    | 0.09           | 0.03  | 0.3                  | 0.44 | 1.71  | 0.83                    | 0.09 | 0.49  | 0.34 | 0.17   |
| Product Analysis      |                       |       |                         |                |       |                      |      |       |                         |      |       |      |        |
| Analyte               | $\text{Na}_2\text{O}$ |       | $\text{Al}_2\text{O}_3$ | $\text{SiO}_2$ | Cl    | $\text{K}_2\text{O}$ |      | CaO   | $\text{Fe}_2\text{O}_3$ |      | ZnO   |      |        |
| Composition (%)       | 0.194                 |       | 99.511                  | 0.204          | 0.029 | 0.011                |      | 0.016 | 0.022                   |      | 0.013 |      |        |

**Table 2** Cost estimation of  $\text{Al}_2\text{O}_3$  powders extraction per kg using WBC as the source.

| Name   | Unit price, \$ | Cost per kg, \$          |
|--|----------------|--------------------------|
| <b>Raw material:</b>   |                |                          |
| WBC  | 1.6 per kg     | 0.9                      |
| NaOH pellet  | 7.06 per kg    | 19.84                    |
| HCl solution   | 7.88 per lit.  | 44.16                    |
| <b>Energy used:</b>  |                |                          |
| Magnetic stirrer, centrifuge, oven, and furnace                  | 0.08 per KW    | 14.07–17.05 <sup>a</sup> |
| <b>Labour cost + others</b>                                      |                | 5.5                      |
| <b>Total cost of <math>\text{Al}_2\text{O}_3</math> (per kg)</b> |                | 84.47–87.45              |

<sup>a</sup> Depends on the applied calcination temperature (500–1200 °C).

the highest percentage of yield was attained for 50 min of reaction time, however, after 35 min of reaction time tiny increase in yield percentage can be seen (0.04–0.11 %). The plausible explanation is that as the reaction time passes, there is more interaction of acid molecules with the targeted particles and after a certain time (i.e., 35 min) when the reaction is nearly completed, the limited accessibility of reactant molecule is not causing enough new interactions (Tantawy and Ali Alomari, 2019). So, considering the more convenient and fullest economical extent viewpoint, a reaction time of 35 min is most favorable in the present conditions.

### 3.4. Effect of NaOH

To check the effect of NaOH on the percent yield of  $\text{Al}_2\text{O}_3$ , four experiments having the amount of NaOH ranging from 230 ml to 260 ml were conducted maintaining other conditions at optimum levels and experimental outcomes are represented in Fig. 2(b). It can be observed that with the addition of NaOH from 230 ml to 250 ml, the percent yield of  $\text{Al}_2\text{O}_3$  increased from 83.9 to 97.80 %. The reason is that when we increase the amount of NaOH, excess NaOH causes more  $\text{Al}(\text{OH})_3$  to react with it and undergoes in solution as  $\text{NaAlO}_2$ . However, with further addition of NaOH (260 ml), the yield remains visibly unchanged since after adding 250 ml, almost all the  $\text{Al}(\text{OH})_3$  is converted to soluble sodium aluminate and so, the percentage of yield remained the same.

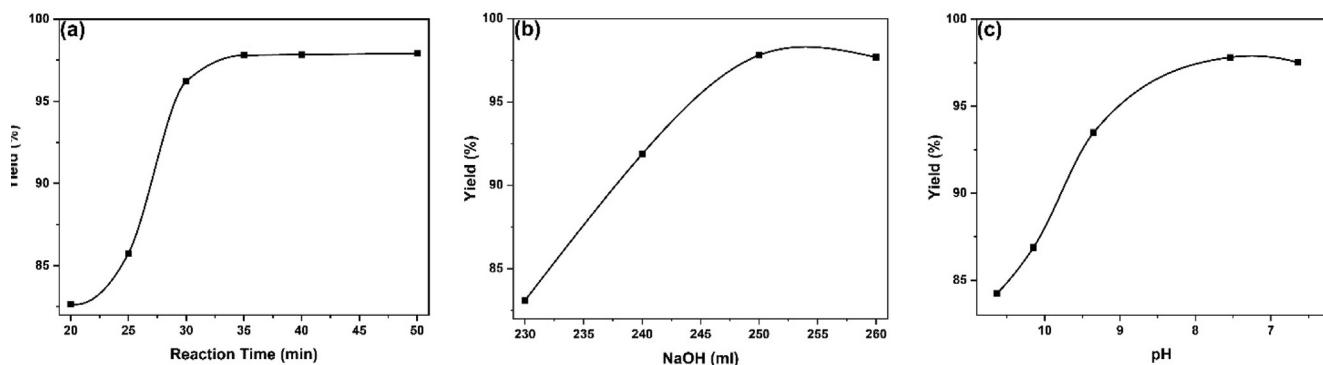
### 3.5. Effect of precipitating agent

Fig. 2(c) provides information about the influence of HCl (precipitating agent) on the yield of the products. For the WBC waste sources, five experiments were carried out having pH adjusted between 10.63 and 6.64 by varying the HCl (1:1) amount of 55-, 60-, 65-, 70-, and 75 ml and keeping the remaining parameters at a constant level. With the decrease of pH between 10.63 and 7.54 by adding HCl (55 ml to 70 ml), the yield percentage escalates from 84.25 % to 97.8 %. This can be attributed to the HCl reaction with excess alkali converted  $\text{NaAlO}_2$  to precipitate as  $\text{Al}(\text{OH})_3$ , thereafter, the pH of the solution decreases, and at pH down to ca. 7.5, the conversion process is almost completed. Further addition of precipitating agent (75 ml HCl), it started to react with  $\text{Al}(\text{OH})_3$ , and some Al underwent again in solution as  $\text{AlCl}_3$ . That is the reason, we observed a slight decrease in percent yield (96.91 %) of  $\text{Al}_2\text{O}_3$  at pH 6.64 (Fig. 2c).

## 4. Characterization of the extracted $\text{Al}_2\text{O}_3$ powders

### 4.1. Thermal analysis

In Fig. 3, the thermal analysis profiles of the extracted intermediate of alumina (non-calcined) dried at 110 °C for 12 hrs. are presented. The TGA thermogram shows three regions of weight loss. The first region of gradual weight loss (~ 5.01 %) can be observed in the temperature region between 33 and 229 °C related to a small endothermic peak at 66 °C which may ascribe to the release of physisorbed water and chemisorbed water, leading toward the transformation of boehmite ( $\gamma\text{-AlOOH}$ ) to alumina ( $\gamma\text{-Al}_2\text{O}_3$ ). The second and drastic weight fall, composed of ca. 27.147 %, takes place in the temperature range of 23–500 °C corresponding to a sharp endothermic trough at 280 °C which may attribute to the breakage of Al-OH bonds (dehydroxylation) during the  $\gamma\text{-AlOOH}$  transition to  $\gamma\text{-Al}_2\text{O}_3$  phase. The final and smallest weight decrement (~ 2.963 %) above 500 °C may associate with the dehydroxylation of the formed gamma-aluminum oxide ( $\gamma\text{-Al}_2\text{O}_3$ ) and subsequent phase transformations of other aluminas. The above-mentioned regions are analogous to the findings of other researchers' works (Asencios and Sun-Kou, 2012; Du et al., 2009; Rinaldi and Schuchardt, 2005; Sarker et al., 2015; Wang et al., 1998). It is noteworthy that the



**Fig. 2** Effect of different reaction parameters on  $\text{Al}_2\text{O}_3$  yield.

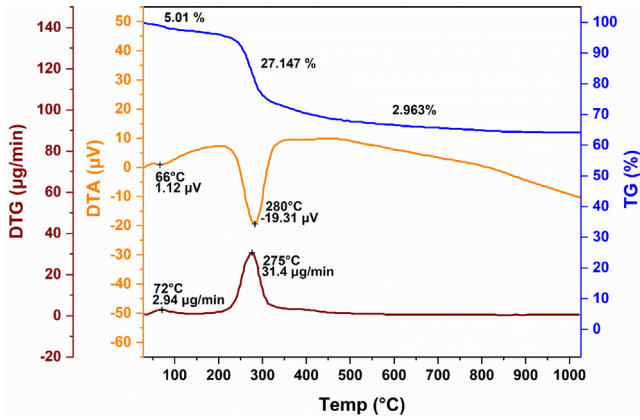


Fig. 3 TG-DTA-DTG profiles of the extracted intermediate of alumina (non-calcined). Structural analysis of  $\text{Al}_2\text{O}_3$  powder.

sum of observed weight loss found ca. 35.12 % which agrees well with the theoretical weight loss of  $\text{Al}(\text{OH})_3$  dehydration about 34.641 % by the stated reaction in Eq. (5). The DTG curve exhibits the highest decomposition rate amounting to 31.4  $\mu\text{g}/\text{min}$  was acquired at 275 °C (Fig. 3).

## 5. Phase characterization

Fig. 4 shows the XRD profiles of extracted alumina powders at different calcination temperatures. Detailed peak positions and indexing information are given in Table S2. For the XRD patterns of the products calcined at 280 and 340 °C, we could observe the peak positions of mixed phases. These could be attributed to bayerite (ICCD PDF card: 00–020-0011), boehmite (ICCD PDF card: 00–021-1307), and  $\gamma\text{-Al}_2\text{O}_3$  (ICCD PDF card: 01–074-4629) phases (Su and Li, 2011; Tripathy et al., 2019; Türk et al., 2020; Yi et al., 2009). As the calcination temperature increased to 500 °C, single-phase  $\gamma\text{-Al}_2\text{O}_3$  was detected, which indicated the complete transformation to  $\gamma\text{-}$

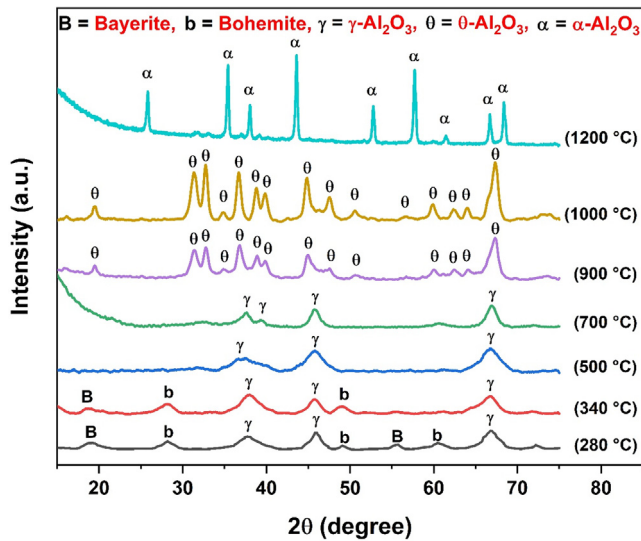


Fig. 4 XRD patterns of WBC derived alumina powders showing different phases at different calcination temperatures.

$\text{Al}_2\text{O}_3$  and supported the findings obtained from TG analysis (Fig. 3). No phase variation except marginal increase of peak intensity was seen for the powder sample calcined at 700 °C (Su and Li, 2011; Zhang et al., 2019). Subsequently, narrow and strong characteristic peaks of the  $\theta\text{-Al}_2\text{O}_3$  phase (ICCD PDF card: 00–023-1009) were detected for the powders calcined at 900 and 1000 °C and have not traced any other alumina or impurity peaks (Gangwar et al., 2014; Sarker et al., 2015). It can be noticed that the metastable  $\delta\text{-Al}_2\text{O}_3$  phase was skipped during the transition of  $\gamma\text{-Al}_2\text{O}_3$  to  $\theta\text{-Al}_2\text{O}_3$ , as reported in the literature (Amirsalari and Farjami Shayesteh, 2015; Gangwar et al., 2014; Nguyen, 2019; Wang et al., 1998), most probably owing to the fact that thermal treatment is needed between 700 and 900 °C. Further raising of calcination temperature up to 1200 °C, only the distinctive sharp peaks of pure  $\alpha\text{-Al}_2\text{O}_3$  (ICCD PDF card: 00–010-0173) emerged with the complete disappearance of  $\theta\text{-Al}_2\text{O}_3$  peaks (Mirjalili et al., 2011; Pepper et al., 2021; Shi et al., 2018).

### 5.1. Assessment of structural parameters

Table 3 represents several physical parameters viz. crystallite size (L), crystallinity (CL), strain ( $\epsilon$ ), dislocation density ( $\delta$ ), and specific surface area (SSA) (S) of WBC derived alumina powders at different calcination temperatures, which are determined using each of the three major diffraction peaks and the following formulas (Barzinjy and Azeez, 2020; Ibrahim and Abu-Ayana, 2008b; Rahman et al., 2020; Singh et al., 2014; Williamson and Smallman, 1956).

$$L = \frac{k\lambda}{\beta \cos\theta} \quad (6)$$

$$CL = \frac{A_c}{A_c + A_a} \times 100 \quad (7)$$

$$\epsilon = \frac{\beta}{4 \tan\theta} \quad (8)$$

$$\delta = \frac{1}{L^2} \quad (9)$$

$$S = \frac{6}{\rho L} \quad (10)$$

Where  $\lambda$  = wavelength of the incident X-ray radiation (=0.15406 nm),  $k$  = Scherrer constant (=0.9),  $\beta$  = full-width of the peak at half-maximum (FWHM) intensity,  $\theta$  = Bragg's angle of diffraction,  $A_c$  = integrated area under the crystalline Peaks,  $A_a$  = integrated area of amorphous halos,  $\rho$  = lattice density (=3.59, 3.616 and 3.989  $\text{gm cm}^{-3}$  for gamma, theta and alpha alumina, respectively).

We can notice from Table 3 that with the increase in heat treatment temperatures, the average sizes of crystal (L) also raise from 10.96 nm to 47.41 nm. The plausible reason is that an increased calcination temperature assists the growth of crystals (Sarker et al., 2015; Toniolo et al., 2005). Meanwhile, the crystallinity values were improved (77.97–91.39 %) which could be further supported by the inverse correlation of strain ( $\epsilon$ ) and dislocation density ( $\delta$ ) against crystallite size. Besides, the obtained  $\epsilon$  (0.00277–0.00815) and  $\delta$  ( $0.45 \times 10^{15}$ – $8.33 \times 10^{15} \text{ m}^{-2}$ ) values implied the high quality and proper chemical stability of extracted alumina powders with a very

**Table 3** Structural parameters and optical property of WBC derived alumina powders at different calcination temperatures.

| Calcination temp. (°C) | Crystallite size (L, nm) | Crystallinity (CL, %) | Strain ( $\epsilon$ , $\times 10^{-3}$ ) | Dislocation density ( $\delta$ , $\times 10^{15} \text{ m}^{-2}$ ) | SSA ( $S$ , $\text{m}^2 \text{ g}^{-1}$ ) | Optical energy ( $E_g$ , eV) |
|------------------------|--------------------------|-----------------------|--|--|---|------------------------------|
| 500 °C                 | 10.96                    | 77.97                 | 8.15                                     | 8.33   | 152.49                                    | 5.187                        |
| 700 °C                 | 11.37                    | 80.65                 | 8.07                                     | 7.74   | 146.99                                    | 4.278                        |
| 900 °C                 | 25.73                    | 90.79                 | 4.24                                     | 1.51   | 64.49                                     | 4.961                        |
| 1000 °C                | 26.34                    | 91.2                  | 3.75                                     | 1.44   | 63  | 4.525                        |
| 1200 °C                | 47.41                    | 91.39                 | 2.77                                     | 0.45   | 31.73                                     | 4.091                        |

few defects per unit volume in the crystal lattice (Amirsalari and Farjami Shayesteh, 2015; Bhoi et al., 2020). The SSA values for different aluminas were found quite large (especially for  $\gamma$ - $\text{Al}_2\text{O}_3$ ) and varied between 31.73–152.49  $\text{m}^2/\text{g}$ . Large SSA is imperative for alumina particles with high catalytic and sensory properties (Ibrahim and Abu-Ayana, 2008b; Yi et al., 2009).

## 6. FT-IR studies

FTIR spectra at 4000–400  $\text{cm}^{-1}$  of alumina powders obtained by calcination at different temperatures are shown in Fig. 5. A distinct characteristic peak is noticed at ca. 564  $\text{cm}^{-1}$  in all samples can be attributed to the stretching vibration of Al-O in the  $\text{AlO}_6$  octahedron ( $\nu\text{AlO}_6$ ). For the alumina samples calcined at 900 °C, 1000 °C, and 1200 °C, a mediocre broad absorption band has appeared which may assign to the stretching vibration mode of tetrahedrally coordinated Al-O ( $\nu\text{AlO}_4$ ). All these peaks apparently confirm the formation of alumina. Besides, the complete evolution of alumina is also corroborated by the missing absorption band at ca. 1080  $\text{cm}^{-1}$  (bending mode of symmetrical Al—O—H for boehmite) in the alumina structure. Following outcomes obtained from FT-IR analysis are well consistent with the other reported works (Ascencios and Sun-Kou, 2012; Hosseini et al., 2011; Kysil et al., 2017; Pan et al., 2013; Tantawy and Ali Alomari, 2019; Yacob et al., 2016; Yang et al., 2010).

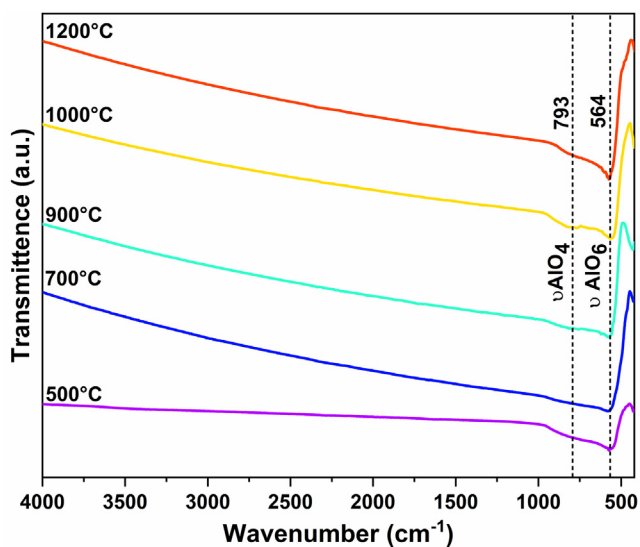


**Fig. 5** FT-IR spectra of WBC derived alumina powders obtained from different calcination temperatures.

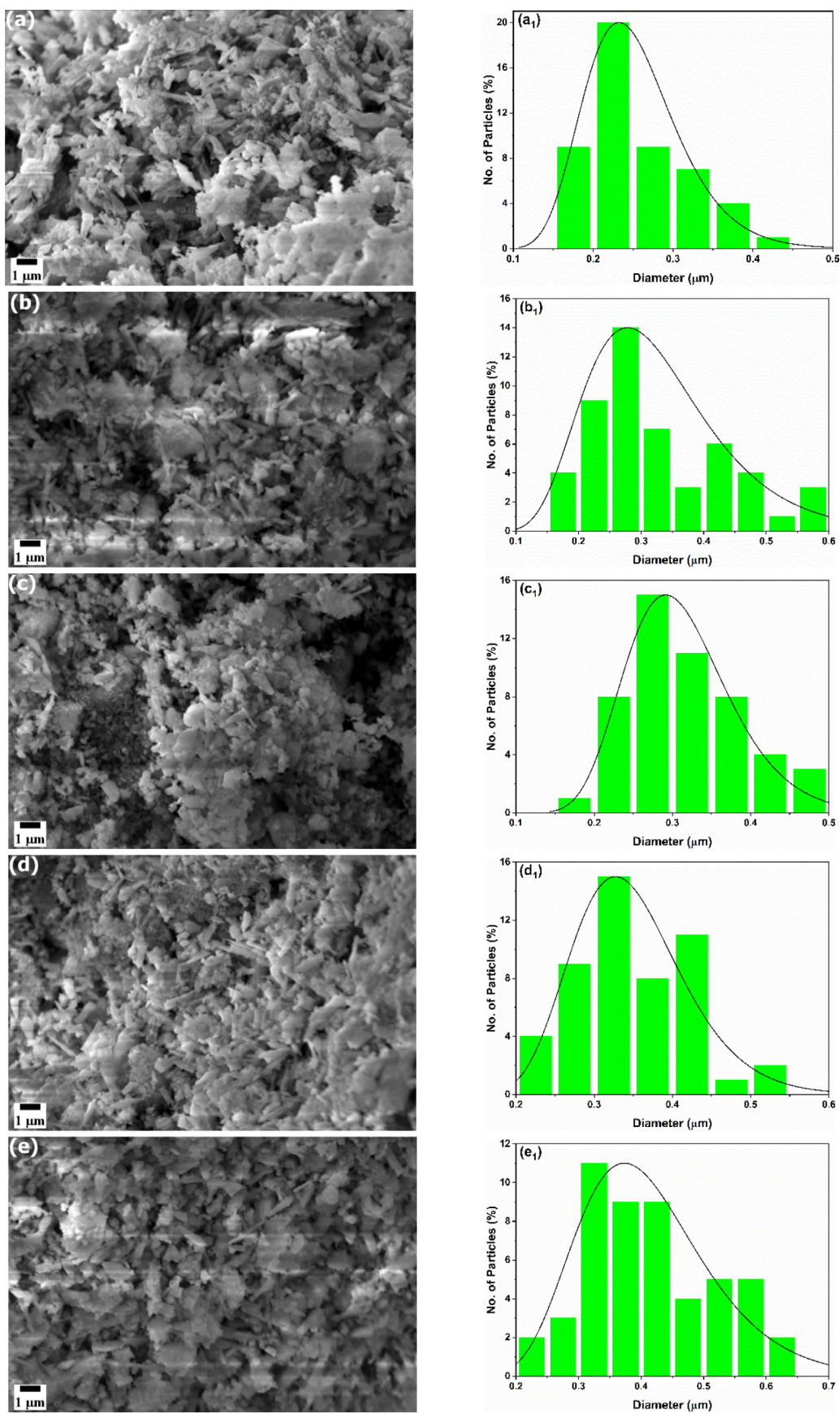
## 7. Surface morphology study

Fig. 6(a)–(e) and (a<sub>1</sub>)–(e<sub>1</sub>) depict the SEM micrographs and particle size distribution (PSD) histograms of the as prepared  $\text{Al}_2\text{O}_3$  powder samples calcinated at different temperatures, respectively. ImageJ (version 1.5c) and OriginPro 2018 (version 9.5.1.195) softwares were applied to determine the average particle size by calculating a count of around 50 particles size from the SEM figure. From SEM analysis, it distinctly revealed that the samples have an agglomerated with irregular outlines and sizes (a typical characteristic of powders prepared by precipitation route) and porous-like surface morphology (Fig. 6 (a<sub>1</sub>–e<sub>1</sub>)). The agglomerates consist of small sub-micron size particles connected by weak forces during the calcination, and some tiny individual alumina particles seemed to be attached to the aggregate structures. The agglomeration tendency may be owing to the high SSA of alumina particles that enable them thermodynamically hectic enough to become agglomerated. It can be observed from Fig. 6 (a<sub>1</sub>–e<sub>1</sub>) and Table 4 that with the increasing calcination temperatures, the average size of fine alumina particles also increased that ranging from 0.23 to 0.38  $\mu\text{m}$  with the narrow PSD.

From SEM micrographs, the pore-size distribution and porosity (i.e., pore area) were statistically checked further from over 250 pores for characterization of calcined  $\text{Al}_2\text{O}_3$  samples, and the outcome is presented in Table 4 and Figure S1. The result showed that for different calcination temperatures, the average pore sizes are between 0.14 and 0.19  $\mu\text{m}$  with a relatively narrow distribution of pore size. Interestingly, similar to the pore size findings, no definite trend in the porosity values was noticed with calcination temperature elevation, and all pore areas are amidst a 5–15 % limit.

## 8. Zeta potential and particle size analysis

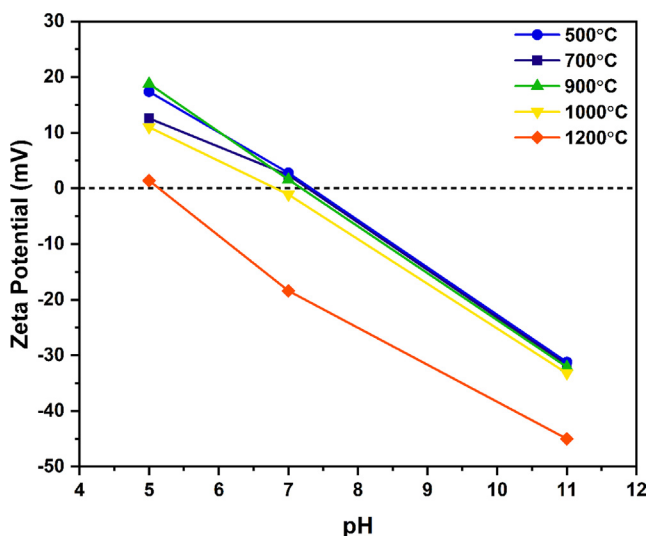
The zeta potential represents the surface charge of the particle in an aqueous medium that can be influenced by the ionic strength and pH of the dispersant. Fig. 7 illustrates the plot of zeta ( $\zeta$ ) potentials vs pH for the WBC derived various aluminas obtained from different calcination temperatures. It could be noticed that the  $\zeta$ -potentials continuously reduced as the pH raised from 5 to 11 and all calcined aluminas were found stable anionically in aqueous dispersion, as corroborated by the high negative  $\zeta$ -potentials (i.e., electrostatic double layer repulsions among the particles that prevent particles aggregation) between  $-31.2$  to  $-45$  mV at pH 11. In general, particles with the  $\zeta$ -potential higher than  $\pm 30$  mV are typically regarded as electrostatically stable (Prabhakar and Samadder, 2018). Meanwhile, increasing the



**Fig. 6** FE-SEM micrographs [(a)-(e)] and corresponding PSD histograms [(a<sub>1</sub>)-(e<sub>1</sub>)] of WBC derived alumina powders at calcination temperatures of 500, 700, 900, 1000 and 1200  $^{\circ}\text{C}$ , respectively.

**Table 4** Different morphological parameter results of the prepared alumina samples calcined at different temperatures.

| Calcination temp. (°C) | Particle size ( $\mu\text{m}$ ) | Pore size ( $\mu\text{m}$ ) | Porosity (%) | Hydrodynamic particle size ( $d$ , $\mu\text{m}$ ) | $\zeta$ -potential at pH 11 ( $Z_p$ , $\mu\text{m}^2$ ) | IEP  |
|------------------------|---------------------------------|-----------------------------|--------------|--|---|------|
| 500 °C                 | $0.225 \pm 0.008$               | $0.192 \pm 0.046$           | 10.51        | 0.426  | -31.2   | 7.32 |
| 700 °C                 | $0.268 \pm 0.008$               | $0.159 \pm 0.02$            | 14.66        | 0.665  | -31.7   | 7.26 |
| 900 °C                 | $0.295 \pm 0.01$                | $0.189 \pm 0.136$           | 11.02        | 0.431  | -32.1   | 7.18 |
| 1000 °C                | $0.34 \pm 0.02$                 | $0.136 \pm 0.028$           | 4.80         | 0.599  | -33.2   | 6.81 |
| 1200 °C                | $0.38 \pm 0.016$                | $0.16 \pm 0.03$             | 12.42        | 4.28   | -45   | 5.15 |

**Fig. 7** Plot of  $\zeta$ -potentials of WBC derived alumina powders obtained from different calcination temperatures as a function of the pH.

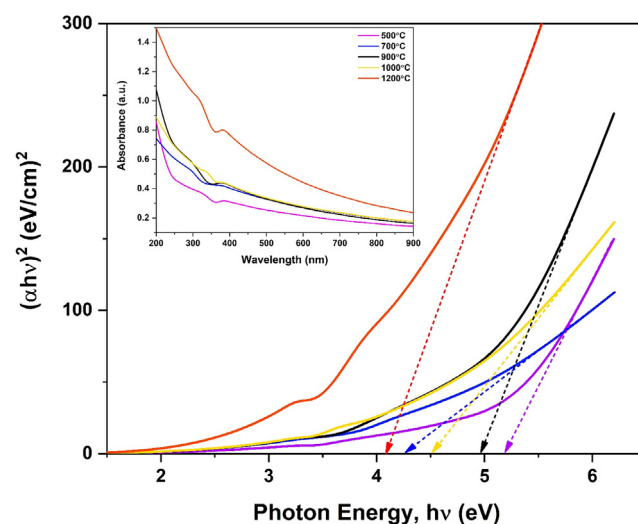
calcination temperature from 500 °C to 1200 °C noticeably induced the shifting of isoelectric points (IEPs) or the point of zero charges (PZCs) to a low pH region (ca. 7.32–5.15). A similar trend of downwards shifting of IEP with increasing calcination temperature was observed by Zhang and coworkers (Zhang et al., 2019). The IEP values for  $\text{Al}_2\text{O}_3$  calcined at 500, 700, 900, 1000, and 1200 °C were 7.32, 7.26, 7.18, 6.81, and 5.15, respectively (Table 4, Fig. 7). Shifting of the IEP values to a lower pH also suggested an increase in the dispersion's stability in a liquid solution with the increase of heat treatment (Cacua et al., 2019; Liao et al., 2009). The hydrodynamic particle sizes of prepared samples were tabulated in Table 4 which is based on the DLS technique and always remain higher than the particle sizes estimated from SEM where the size of the particle is pertaining to dehydrated sample (Basak et al., 2022; Bootz et al., 2004). It can be observed that the trend of rising the particle size with temperature (Ahmed et al., 2015; Rincón Joya et al., 2019) nearly supports a similar pattern from the SEM portions. The  $\text{Al}_2\text{O}_3$  particles calcined from 500 to 1200 °C show z-average (mean hydrodynamic diameter) values of particles size ranging between 0.426 and 4.24  $\mu\text{m}$  (Table 4) (Berg et al., 2009; Bhoi et al., 2020).

## 9. Optical property studies

Spectral analysis by UV–vis spectroscopy can aid to apprehend the relevant electronic structure of the material's optical

band gap and this type of study is a matter of considerable research (Chand et al., 2017). In the inset of Fig. 8 the UV–vis absorption spectra of the  $\text{Al}_2\text{O}_3$  samples processed under different calcination temperatures are presented and the Tauc's plot for estimating the optical band gap of corresponding samples from UV–visible spectroscopy data is shown in Fig. 8. From these spectral curves a characteristic absorption peak at  $\sim 382$  nm is observed in UV-region and steady absorption in the visible or NIR region. It is also noticeable that with the reduction of calcination temperatures (i.e., decrement in crystallite or particle size), the absorption edge is marginally shifted towards the shorter wavelength (i.e., blue shift) which is a corroboration of the optical quantum confinement effect (QCE) and also specifies the dependence of absorption positions on the sizes and morphologies of  $\text{Al}_2\text{O}_3$  (Fig. 8 inset) (Amirsalari and Farjami Shayesteh, 2015; Huang et al., 2007). The high absorption preference in the UV region and absence of absorption peak in the visible wavelength of synthesized powders implies the consideration of the potential photocatalytic application and distinct reflective feature for visible lights (Halder and Bandyopadhyay, 2020; Rahman and Jayaganthan, 2015).

The absorption capacity of alumina in the UV region is connected to the optical band gap energy ( $E_g$ ). The  $E_g$  values can be estimated through Tauc's relation. According to Tauc's argument, the relation between optical absorption coefficient

**Fig. 8** Typical Tauc's plot [ $(\alpha h\nu)^2$  vs  $h\nu$ ] of WBC derived alumina powders processed under different calcination temperatures. The inset shows the UV–vis spectra of corresponding synthesized samples.

( $\alpha$ ) and photon energy ( $h\nu$ ) is expressed as follows (Tauc and Menth, 1972):

$$\alpha = \frac{A}{h\nu} (h\nu - E_g)^m \quad (11)$$

$$(\alpha h\nu)^{1/m} = A(h\nu - E_g) \quad (12)$$

where  $A$  = energy independent constant (band tailing parameter),  $E_g$  = energy of the optical band gap, and  $m$  = transition power factor which is related to the nature of the material and photon transition mode. The absorption coefficient ( $\alpha$ ) is calculated by the following equation (Amirsalari and Farjami Shayesteh, 2015; Azam et al., 2011):

$$\alpha = 2.303 \left( \frac{A_b}{t} \right) \quad (13)$$

where  $A_b$  = absorbance or absorption index and  $t$  = cuvette thickness, generally 1 cm.

For our crystalline materials, direct allowed transition ( $m = 0.5$ ) is valid. Hence, putting  $m = 0.5$  in Eq. (12), we have:

$$(\alpha h\nu)^2 = A(h\nu - E_g) \quad (14)$$

Therefore, plotting a graph between  $(\alpha h\nu)^2$  and the photon energy ( $h\nu$ ), known as Tauc's plot, provides a straight line in a particular region. The extrapolation of this straight line to intersect the energy ( $h\nu$ ) axis at  $(\alpha h\nu)^2 = 0$  gives the value of the corresponding direct energy band gap,  $E_g$  (Fig. 8) (Halder and Bandyopadhyay, 2020).

The graphically calculated  $E_g$  values for 500–1200 °C calcined alumina samples were compiled in Table 4. The obtained  $E_g$  values were found between the 5.19–4.09 eV range, which is nearly matched with other researchers' findings (Amirsalari and Farjami Shayesteh, 2015; Dhonge et al., 2011; Gangwar et al., 2014; Jbara et al., 2017). Furthermore, the values of  $E_g$  usually decreased with increasing the calcination temperatures except for the 700 °C calcined one. This may be due to the QCE since particles size is increased with the elevated heat treatment (Dhonge et al., 2011; Farahmandjou and Golabiyani, 2015; Singh et al., 2014; Wang and Herron, 1991). The estimated small  $E_g$  values would be instrumental in enhancing the photocatalytic property of  $Al_2O_3$  material.

## 10. Conclusions

Recycling of waste beverage cans is an important aspect of waste management by reducing the necessity for incineration or landfilling of these enormous solid wastes and exploiting them in an alternative feasible way. This paper reports a successful extraction of single-phase aluminas from easily obtainable WBCs through a facile chemical precipitation technique at different calcination temperatures (500–1200 °C). The extraction process was optimized by investigating and changing the different reaction parameters. The presence of single-phase  $\gamma$ - $Al_2O_3$  at 500 °C and 700 °C,  $\theta$ - $Al_2O_3$  at 900 °C and 1000 °C, and  $\alpha$ - $Al_2O_3$  at 1200 °C were confirmed by X-ray diffraction studies. The structural parameters viz. crystallite size, crystallinity rises with elevated temperature and vice-versa for strain, dislocation density, and SSA. The morphological analysis demonstrated the agglomeration of the synthesized alumina and the average size of the fine particles increases with calcination temperature having narrow distribution ranging from 0.23 to 0.38  $\mu$ m. However, interestingly, no definite trend

was obtained for pore size and porosity with calcination temperature.  $\zeta$ -potentials for all the samples were between  $-31$  to  $-45$  range with a low IEP which is typically regarded as electrostatically stable in the aqueous medium. The optical property measurements revealed that the prepared alumina particles would be viable in optoelectronics applications. In particular, the  $\gamma$ - $Al_2O_3$  obtained at 500 °C and 700 °C can be applied as catalyst and humidity sensor,  $\theta$ - $Al_2O_3$  (900 °C and 1000 °C) is suitable for optical sensor and dielectronic fields, and  $\alpha$ - $Al_2O_3$  (1200 °C) can be used in advanced ceramics, high temperature electrical insulators, high voltage insulators, and coatings.

## Declaration of Competing Interest

The authors declare that they have no known competing financial interests or personal relationships that could have appeared to influence the work reported in this paper.

## Acknowledgments

The authors acknowledge the Institute of Glass and Ceramic Research & Testing (IGCRT), Bangladesh Council of Scientific and Industrial Research (BCSIR), Dhaka-1205, Bangladesh for financial support and facilities. The authors also thank Glass Research Division, IGCRT, BCSIR, Pilot Plant and Process Development Centre (PP&PDC), BCSIR, Central Analytical and Research Facilities (CARF), BCSIR and Institute of Fuel Research and Development (IFRD), BCSIR, Dhaka-1205, Bangladesh for their supports.

## Appendix A. Supplementary material

Supplementary data to this article can be found online at <https://doi.org/10.1016/j.arabjc.2022.104518>.

## References

- Adans, Y.F., Martins, A.R., Coelho, R.E., Virgens, C.F. das, Ballarini, A.D., Carvalho, L.S., 2016. A simple way to produce  $\gamma$ -alumina from aluminum cans by precipitation reactions. *Materials Research* 19, 977–982.
- Alfa Aesar, 2022. Aluminum oxide, gamma-phase, 99.97% (metals basis) [WWW Document]. URL <https://www.alfa.com/en/catalog/039812/?fbclid=IwAR2fk7bO-B6NfJooOyGiqd-jxf3359BnH7yjDbE5Ruw7HPAhJkBhHoXZQcdQ> (accessed 12.6.22).
- Ahmed, Y.M.Z., El-Sheikh, S.M., Zaki, Z.I., 2015. Changes in hydroxyapatite powder properties via heat treatment. *Bulletin of Materials Science* 38, 1807–1819.
- Amirsalari, A., Farjami Shayesteh, S., 2015. Effects of pH and calcination temperature on structural and optical properties of alumina nanoparticles. *Superlattices Microstruct* 82, 507–524. <https://doi.org/10.1016/j.spmi.2015.01.044>.
- Ananthapadmanabhan, P. v., Thiagarajan, T.K., Sreekumar, K.P., Venkatramani, N., 2004. Formation of nano-sized alumina by in-flight oxidation of aluminium powder in a thermal plasma reactor. *Scr Mater* 50, 143–147. <https://doi.org/10.1016/J.SCRIPMAT.2003.09.001>
- Asencios, Y.J.O., Sun-Kou, M.R., 2012. Synthesis of high-surface-area  $\gamma$ - $Al_2O_3$  from aluminum scrap and its use for the adsorption of metals: Pb(II), Cd(II) and Zn(II). *Appl Surf Sci* 258, 10002–10011. <https://doi.org/10.1016/j.apsusc.2012.06.063>.

- Azam, A., Jawad, A., Ahmed, A.S., Chaman, M., Naqvi, A.H., 2011. Structural, optical and transport properties of Al<sub>3+</sub> doped BiFeO<sub>3</sub> nanopowder synthesized by solution combustion method. *J Alloys Compd* 509, 2909–2913.
- Barzinjy, A.A., Azeez, H.H., 2020. Green synthesis and characterization of zinc oxide nanoparticles using Eucalyptus globulus Labill. leaf extract and zinc nitrate hexahydrate salt. *SN Appl Sci* 2, 991. <https://doi.org/10.1007/s42452-020-2813-1>.
- Basak, M., Rahman, M.L., Ahmed, M.F., Biswas, B., Sharmin, N., 2022. The use of X-ray diffraction peak profile analysis to determine the structural parameters of cobalt ferrite nanoparticles using Debye-Scherrer, Williamson-Hall, Halder-Wagner and Size-strain plot: Different precipitating agent approach. *J Alloys Compd* 895. <https://doi.org/10.1016/J.JALLCOM.2021.162694>
- Berg, J.M., Romoser, A., Banerjee, N., Zebda, R., Sayes, C.M., 2009. The relationship between pH and zeta potential of ~ 30 nm metal oxide nanoparticle suspensions relevant to in vitro toxicological evaluations. <http://dx.doi.org/10.3109/17435390903276941> 3, 276–283. <https://doi.org/10.3109/17435390903276941>.
- Bhoi, N.K., Singh, H., Pratap, S., 2020. Synthesis and Characterization of Alumina Nanoparticles: A Case Study. *Journal of The Institution of Engineers (India): Series C* 101, 407–413. <https://doi.org/10.1007/s40032-019-00542-w>.
- Bootz, A., Vogel, V., Schubert, D., Kreuter, J., 2004. Comparison of scanning electron microscopy, dynamic light scattering and analytical ultracentrifugation for the sizing of poly(butyl cyanoacrylate) nanoparticles. *European Journal of Pharmaceutics and Biopharmaceutics* 57, 369–375. [https://doi.org/10.1016/S0939-6411\(03\)00193-0](https://doi.org/10.1016/S0939-6411(03)00193-0).
- Busca, G., 2014. Structural, Surface, and Catalytic Properties of Aluminas. *Advances in Catalysis* 57, 319–404. <https://doi.org/10.1016/B978-0-12-800127-1.00003-5>.
- Cacua, K., Ordoñez, F., Zapata, C., Herrera, B., Pabón, E., Buitrago-Sierra, R., 2019. Surfactant concentration and pH effects on the zeta potential values of alumina nanofluids to inspect stability. *Colloids Surf A Physicochem Eng Asp* 583. <https://doi.org/10.1016/J.COLSURFA.2019.123960>
- Chand, P., Vaish, S., Kumar, P., 2017. Structural, optical and dielectric properties of transition metal (MFe<sub>2</sub>O<sub>4</sub>; M = Co, Ni and Zn) nanoferrites. *Physica B Condens Matter* 524, 53–63. <https://doi.org/10.1016/J.PHYSB.2017.08.060>.
- Chen, C., Ding, Z., Tan, Q., Qi, H., He, Y., 2014. Preparation of nano  $\alpha$ -alumina powder and wear resistance of nanoparticles reinforced composite coating. *Powder Technol* 257, 83–87. <https://doi.org/10.1016/J.POWTEC.2014.02.059>.
- Chotisuwan, S., Sirirak, A., Har-Wae, P., Wittayakun, J., 2012. Mesoporous alumina prepared from waste aluminum cans and used as catalytic support for toluene oxidation. *Mater Lett* 70, 125–127. <https://doi.org/10.1016/J.MATLET.2011.11.077>.
- Council, N.R., 1999. Separation Technologies for the Industries of the Future. *Separation Technologies for the Industries of the Future*. <https://doi.org/10.17226/6388>.
- Dhonge, B.P., Mathews, T., Sundari, S.T., Thinaharan, C., Kamrudin, M., Dash, S., Tyagi, A.K., 2011. Spray pyrolytic deposition of transparent aluminum oxide (Al<sub>2</sub>O<sub>3</sub>) films. *Appl Surf Sci* 258, 1091–1096. <https://doi.org/10.1016/J.APSUSC.2011.09.040>.
- Du, X., Wang, Y., Su, X., Li, J., 2009. Influences of pH value on the microstructure and phase transformation of aluminum hydroxide. *Powder Technol* 192, 40–46. <https://doi.org/10.1016/j.powtec.2008.11.008>.
- Durbin, D.J., Malardier-Jugroot, C., 2013. Review of hydrogen storage techniques for on board vehicle applications. *Int J Hydrogen Energy* 38, 14595–14617.
- Dutta, S., 2014. A review on production, storage of hydrogen and its utilization as an energy resource. *Journal of Industrial and Engineering Chemistry* 20, 1148–1156.
- El-Amir, A.A.M., Ewais, E.M.M., Abdel-Aziem, A.R., Ahmed, A., El-Anadouli, B.E.H., 2016. Nano-alumina powders/ceramics derived from aluminum foil waste at low temperature for various industrial applications. *J Environ Manage* 183, 121–125. <https://doi.org/10.1016/J.JENVMAN.2016.08.072>.
- Farahmandjou, M., Golabiyani, N., 2015. New pore structure of nano-alumina (Al<sub>2</sub>O<sub>3</sub>) prepared by sol gel method. *Journal of Ceramic Processing Research* 16, 1–4.
- Feng, G., Jiang, W., Liu, J., Li, C., Zhang, Q., Miao, L., Wu, Q., 2017. Novel nonaqueous precipitation synthesis of alumina powders. *Ceram Int* 43, 13461–13468. <https://doi.org/10.1016/J.CERAMINT.2017.07.050>.
- Fisher-Scientific, 2022. Alumina, Dry Powder (Type A) [WWW Document]. URL <https://www.fishersci.com/shop/products/alumina-dry-powder-type-a-fisher-chemical/A447500> (accessed 2.5.22).
- Gangwar, J., Gupta, B.K., Kumar, P., Tripathi, S.K., Srivastava, A. K., 2014. Time-resolved and photoluminescence spectroscopy of  $\theta$ -Al<sub>2</sub>O<sub>3</sub> nanowires for promising fast optical sensor applications. *Dalton Transactions* 43, 17034–17043. <https://doi.org/10.1039/c4dt01831a>.
- Ghanizadeh, S., Bao, X., Vaidhyathan, B., Binner, J., 2014. Synthesis of nano  $\alpha$ -alumina powders using hydrothermal and precipitation routes: a comparative study. *Ceram Int* 40, 1311–1319. <https://doi.org/10.1016/J.CERAMINT.2013.07.011>.
- Hakkar, S., Achache, S., Sanchette, F., Mekhalif, Z., Kamoun, N., Boumaza, A., 2019. Characterization by Photoluminescence and Raman Spectroscopy of the Oxide Scales Grown on the PM2000 at High Temperatures. <https://doi.org/10.1142/S2251237319500035> 07, 1950003. <https://doi.org/10.1142/S2251237319500035>.
- Halder, R., Bandyopadhyay, S., 2020. Effect of cation ratio on microstructure and optical absorbance of magnesium aluminate spinel. *Mater Res Express* 7, 15065.
- Hosseini, S.A., Niaei, A., Salari, D., 2011. Production of  $\gamma$ -Al<sub>2</sub>O<sub>3</sub> from Kaolin. *Open J Phys Chem* 01, 23–27. <https://doi.org/10.4236/ojpc.2011.12004>.
- Huang, C.L., Wang, J.J., Yen, F.S., Huang, C.Y., 2008. Microwave dielectric properties and sintering behavior of nano-scaled ( $\alpha$  +  $\theta$ )-Al<sub>2</sub>O<sub>3</sub> ceramics. *Mater Res Bull* 43, 1463–1471. <https://doi.org/10.1016/J.MATERRESBULL.2007.06.032>.
- Huang, K. long, Yin, L. guo, Liu, S. qin, Li, C. jian, 2007. Preparation and formation mechanism of Al<sub>2</sub>O<sub>3</sub> nanoparticles by reverse microemulsion. *Transactions of Nonferrous Metals Society of China* 17, 633–637. [https://doi.org/10.1016/S1003-6326\(07\)60147-2](https://doi.org/10.1016/S1003-6326(07)60147-2).
- Hurtado, P., Ordóñez, S., Vega, A., Díez, F.v., 2004. Catalytic combustion of methane over commercial catalysts in presence of ammonia and hydrogen sulphide. *Chemosphere* 55, 681–689. <https://doi.org/10.1016/J.CHEMOSPHERE.2003.10.068>.
- Ibrahim, D.M., Abu-Ayana, Y.M., 2008a. Preparation and characterization of ultrafine alumina via sol-gel polymeric route. *Mater Chem Phys* 111, 326–330. <https://doi.org/10.1016/J.MATCHEMPHYS.2008.04.023>.
- Ibrahim, D.M., Abu-Ayana, Y.M., 2008b. Preparation and characterization of ultrafine alumina via sol-gel polymeric route. *Mater Chem Phys* 111, 326–330. <https://doi.org/10.1016/j.matchemphys.2008.04.023>.
- Jbara, A.S., Othaman, Z., Saeed, M.A., 2017. Structural, morphological and optical investigations of  $\theta$ -Al<sub>2</sub>O<sub>3</sub> ultrafine powder. *J Alloys Compd* 718, 1–6.
- Jolly, B.M., Bhattacharya, S.S., 2018. Synthesis of nanocrystalline alumina (Al<sub>2</sub>O<sub>3</sub>) particles from an aqueous precursor by flame-assisted spray pyrolysis. *Mater Today Proc* 5, 10023–10027. <https://doi.org/10.1016/J.MATPR.2017.10.201>.
- Kelekanjeri, V.S.K.G., Carter, W.B., Hampikian, J.M., 2006. Deposition of  $\alpha$ -alumina via combustion chemical vapor deposition. *Thin Solid Films* 515, 1905–1911. <https://doi.org/10.1016/J.TSF.2006.07.033>.
- Kysil, D.V., Vasin, A.V., Sevostianov, S.V., Degoda, V.Y., Strelchuk, V.V., Naseka, V.M., Piryatinski, Y.P., Tertykh, V.A., Nazarov, A. N., Lysenko, V.S., 2017. Formation and Luminescent Properties of

- Al<sub>2</sub>O<sub>3</sub>:SiOC Nanocomposites on the Base of Alumina Nanoparticles Modified by Phenyltrimethoxysilane. *Nanoscale Res Lett* 12, 1–5. <https://doi.org/10.1186/s11671-017-2245-z>.
- Lafficher, R., Digne, M., Salvatori, F., Boualleg, M., Colson, D., Puel, F., 2017. Development of new alumina precipitation routes for catalysis applications. *J Cryst Growth* 468, 526–530. <https://doi.org/10.1016/J.JCRYSGRO.2016.11.092>.
- Levin, I., Brandon, D., 1998. Metastable Alumina Polymorphs: Crystal Structures and Transition Sequences. *Journal of the American Ceramic Society* 81, 1995–2012. <https://doi.org/10.1111/J.1151-2916.1998.TB02581.X>.
- Liao, D.L., Wu, G.S., Liao, B.Q., 2009. Zeta potential of shape-controlled TiO<sub>2</sub> nanoparticles with surfactants. *Colloids Surf A Physicochem Eng Asp* 348, 270–275. <https://doi.org/10.1016/J.COLSURFA.2009.07.036>.
- Marsh, K., Bugusu, B., 2007. Food packaging—roles, materials, and environmental issues. *J Food Sci* 72, R39–R55.
- Matori, K.A., Wah, L.C., Hashim, M., Ismail, I., Mohd Zaid, M.H., 2012. Phase transformations of  $\alpha$ -alumina made from waste aluminum via a precipitation technique. *Int J Mol Sci* 13, 16812–16821. <https://doi.org/10.3390/IJMS131216812>.
- MIC, 2022. Gamma Alumina Powder, Industrial grade [WWW Document]. URL <https://chuangsenkeji.en.made-in-china.com/product/tBDQYpLOviRz/China-High-Purity-Nano-Alumina-Powder-Gamma-Alumina-Powder-with-Best-Alumina-Powder-Price.html> (accessed 12.6.22).
- Mirjalili, F., Mohamad, H., Chuah, L., 2011. Preparation of nano-scale  $\alpha$ -Al<sub>2</sub>O<sub>3</sub> powder by the sol-gel method. *Ceramics-Silikáty*.
- Nguyen, T.T.N.M.S., 2019. Recovery of Alumina from Sodium Hydroxide Leaching Solution by Precipitation with Hydrogen Peroxide. *Resources Recycling* 28, 23–29. <https://doi.org/10.7844/KIRR.2019.28.4.23>.
- Osman, A.I., Abu-Dahrieh, J.K., McLaren, M., Laffir, F., Nockemann, P., Rooney, D., 2017. A Facile Green Synthetic Route for the Preparation of Highly Active  $\gamma$ -Al<sub>2</sub>O<sub>3</sub> from Aluminum Foil Waste. *Scientific Reports* 2017 7:1 7, 1–11. <https://doi.org/10.1038/s41598-017-03839-x>.
- Pan, F., Lu, X., Wang, T., Wang, Y., Zhang, Z., Yan, Y., Yang, S., 2013. Synthesis of large-mesoporous  $\gamma$ -Al<sub>2</sub>O<sub>3</sub> from coal-series kaolin at room temperature. *Mater Lett* 91, 136–138. <https://doi.org/10.1016/j.matlet.2012.09.052>.
- Pepper, R.A., Perenlei, G., Martens, W.N., Couperthwaite, S.J., 2021. High purity alumina synthesised from iron rich clay through a novel and selective hybrid ammonium alum process. *Hydrometallurgy* 204, <https://doi.org/10.1016/J.HYDROMET.2021.105728>.
- Piriyawong, V., Thongpool, V., Asanithi, P., Limsuwan, P., 2012. Preparation and characterization of alumina nanoparticles in deionized water using laser ablation technique. *J Nanomater* 2012. <https://doi.org/10.1155/2012/819403>.
- Prabhakar, R., Samadder, S.R., 2018. Low cost and easy synthesis of aluminium oxide nanoparticles for arsenite removal from groundwater: A complete batch study. *J Mol Liq* 250, 192–201. <https://doi.org/10.1016/j.molliq.2017.11.173>.
- Rahman, L., Bhattacharjee, S., Islam, S., Zahan, F., Biswas, B., Sharmin, N., 2020. A study on the preparation and characterization of maghemite ( $\gamma$ -Fe<sup><sup>2</sup><sup>+</sup>O<sup>3</sup><sup>+</sup>) particles from iron-containing waste materials. *Journal of Asian Ceramic Societies*, 1–12.</sup>
- Rahman, A., Jayaganthan, R., 2015. Study of photocatalyst magnesium aluminate spinel nanoparticles. *Journal of Nanostructure in Chemistry* 2015 5:2 5, 147–151. <https://doi.org/10.1007/S40097-014-0135-9>.
- ReportLinker, 2021. Global Aluminum Cans Market - Growth, Trends, COVID-19 Impact, and Forecasts (2021 - 2026).
- Rinaldi, R., Schuchardt, U., 2005. On the paradox of transition metal-free alumina-catalyzed epoxidation with aqueous hydrogen peroxide. *J Catal* 236, 335–345. <https://doi.org/10.1016/j.jcat.2005.10.007>.
- Rincón Joya, M., Barba Ortega, J., Malafatti, J.O.D., Paris, E.C., 2019. Evaluation of Photocatalytic Activity in Water Pollutants and Cytotoxic Response of  $\alpha$ -Fe<sub>2</sub>O<sub>3</sub> Nanoparticles. *ACS Omega* 4, 17477–17486. [https://doi.org/10.1021/ACSOMEGA.9B02251/SUPPL\\_FILE/AO9B02251\\_SI\\_001.PDF](https://doi.org/10.1021/ACSOMEGA.9B02251/SUPPL_FILE/AO9B02251_SI_001.PDF).
- Risonarta, V.Y., Anggono, J., Suhendra, Y.M., Nugrowibowo, S., Jani, Y., 2019. Strategy to Improve Recycling Yield of Aluminium Cans. *E3S Web of Conferences* 130, 01033. <https://doi.org/10.1051/E3SCONF/201913001033>.
- Roslyakov, I.V., Gordeeva, E.O., Napolskii, K.S., 2017. Role of Electrode Reaction Kinetics in Self-Ordering of Porous Anodic Alumina. *Electrochim Acta* 241, 362–369. <https://doi.org/10.1016/J.ELECTACTA.2017.04.140>.
- Saha, D., Ghara, D.K., Pal, M., 2016. Nanoporous  $\gamma$ -alumina based novel sensor to detect trace moisture in high temperature and high pressure environment. *Sens Actuators B Chem* 222, 1043–1049. <https://doi.org/10.1016/J.SNB.2015.09.068>.
- Sarker, M.S.R., Alam, M.Z., Qadir, M.R., Gafur, M.A., Moniruzzaman, M., 2015. Extraction and characterization of alumina nanopowders from aluminum dross by acid dissolution process. *International Journal of Minerals, Metallurgy and Materials* 22, 429–436. <https://doi.org/10.1007/s12613-015-1090-2>.
- Sercombe, T.B., 2010. Laser sintering and rapid prototyping of aluminium. *Fundamentals of Aluminium Metallurgy: Production, Processing and Applications* 702–718. <https://doi.org/10.1533/9780857090256.3.702>.
- Shi, R., Shang, Y., Zhang, Y., Wang, P., Zhang, A., Yang, P., 2018. Synthesis of ultrafine  $\alpha$ -Al<sub>2</sub>O<sub>3</sub> powder by two-step hydrolysis. *Ceram Int* 44, 3741–3750. <https://doi.org/10.1016/j.ceramint.2017.11.157>.
- Sigma-Aldrich, 2022a. Alumina powder, 45 micron particle size [WWW Document]. URL <https://www.sigmaaldrich.com/US/en/product/aldrich/gf12944190> (accessed 2.4.22).
- Sigma-Aldrich, 2022b. Alumina powder, 45 mean particle size (micron) [WWW Document]. URL <https://www.sigmaaldrich.com/US/en/product/aldrich/gf92436026> (accessed 2.5.22).
- Sigma-Aldrich, 2022c. Gamma alumina powder, 0.1 max mean particle size (micron) [WWW Document]. URL <https://www.sigmaaldrich.com/US/en/product/aldrich/gf29729650> (accessed 2.4.22).
- Singh, A., Singh, S., Joshi, B.D., Shukla, A., Yadav, B.C., Tandon, P., 2014. Synthesis, characterization, magnetic properties and gas sensing applications of ZnxCu<sub>1-x</sub>Fe<sub>2</sub>O<sub>4</sub> (0.0 ≤ x ≤ 0.8) nanocomposites. *Mater Sci Semicond Process* 27, 934–949. <https://doi.org/10.1016/j.mssp.2014.08.029>.
- Su, X., Li, J., 2011. Low Temperature Synthesis of Single-crystal Alpha Alumina Platelets by Calcining Bayerite and Potassium Sulfate. *J Mater Sci Technol* 27, 1011–1015. [https://doi.org/10.1016/S1005-0302\(11\)60179-5](https://doi.org/10.1016/S1005-0302(11)60179-5).
- Suchanek, W.L., 2010. Hydrothermal Synthesis of Alpha Alumina ( $\alpha$ -Al<sub>2</sub>O<sub>3</sub>) Powders: Study of the Processing Variables and Growth Mechanisms. *Journal of the American Ceramic Society* 93, 399–412. <https://doi.org/10.1111/J.1151-2916.2009.03399.X>.
- MSE Supplies, 2022. Alpha Aluminum Oxide (Alumina) Al<sub>2</sub>O<sub>3</sub> Powder 99.999% [WWW Document]. URL <https://www.msesupplies.com/products/5n-alpha-aluminum-oxide-alumina-al2o3-powder-1-2-um-d50-ultra-high-purity-99-999-metal-basis?variant=12231523139642> (accessed 12.6.22).
- Suryanarayana, C., 2005. Recent Developments in Nanostructured Materials. *Adv Eng Mater* 7, 983–992. <https://doi.org/10.1002/ADEM.200500135>.
- Tantawy, M.A., Ali Alomari, A., 2019. Extraction of Alumina from Nawan Kaolin by Acid Leaching. *Oriental Journal of Chemistry* 35, 1013–1021. <https://doi.org/10.13005/ojc/350313>.

- Tauc, J., Menth, A., 1972. States in the gap. *J Non Cryst Solids* 8, 569–585.
- Temuujin, J., Jadambaa, T., Mackenzie, K.J.D., Angerer, P., Porte, F., Riley, F., 2000. Thermal formation of corundum from aluminium hydroxides prepared from various aluminium salts. *Bulletin of Materials Science* 23:4 23, 301–304. <https://doi.org/10.1007/BF02720086>.
- Theiss, F.L., Ayoko, G.A., Frost, R.L., 2016. Synthesis of layered double hydroxides containing  $Mg^{2+}$ ,  $Zn^{2+}$ ,  $Ca^{2+}$  and  $Al^{3+}$  layer cations by co-precipitation methods—A review. *Appl Surf Sci* 383, 200–213. <https://doi.org/10.1016/J.APSUSC.2016.04.150>.
- Tok, A.I.Y., Boey, F.Y.C., Zhao, X.L., 2006. Novel synthesis of  $Al_2O_3$  nano-particles by flame spray pyrolysis. *J Mater Process Technol* 178, 270–273. <https://doi.org/10.1016/J.JMATPROTEC.2006.04.007>.
- Toniolo, J.C., Lima, M.D., Takimi, A.S., Bergmann, C.P., 2005. Synthesis of alumina powders by the glycine-nitrate combustion process. *Mater Res Bull* 40, 561–571. <https://doi.org/10.1016/j.materresbull.2004.07.019>.
- Touzin, M., Goeriot, D., Guerret-Piécourt, C., Juvé, D., Fitting, H. J., 2010. Alumina based ceramics for high-voltage insulation. *J Eur Ceram Soc* 30, 805–817. <https://doi.org/10.1016/J.JEURCERAMSOC.2009.09.025>.
- Tripathy, A.K., Mahalik, S., Sarangi, C.K., Tripathy, B.C., Sanjay, K., Bhattacharya, I.N., 2019. A pyro-hydrometallurgical process for the recovery of alumina from waste aluminium dross. *Miner Eng* 137, 181–186. <https://doi.org/10.1016/J.MINENG.2019.04.009>.
- Türk, M., Altner, M., Top, S., Karaca, S., Boucekrit, C., 2020. Production of alpha-alumina from black aluminum dross using NaOH leaching followed by calcination. *JOM* 72, 3358–3366.
- Wang, J.A., Bokhimi, X., Morales, A., Novaro, O., López, T., Gómez, R., 1998. Aluminum local environment and defects in the crystalline structure of sol-gel alumina catalyst. *Journal of Physical Chemistry B* 103, 299–303. <https://doi.org/10.1021/jp983130r>.
- Wang, Y., Herron, N., 1991. Nanometer-sized semiconductor clusters: materials synthesis, quantum size effects, and photophysical properties. *J Phys Chem* 95, 525–532.
- Wang, H., Li, L., Wei, X., Hou, X., Li, M., Wu, X., Li, Y., te Lin, C., Jiang, N., Yu, J., 2021. Combining Alumina Particles with Three-Dimensional Alumina Foam for High Thermally Conductive Epoxy Composites. *ACS Appl Polym Mater* 3, 216–225. [https://doi.org/10.1021/ACSAPM.0C01055/SUPPL\\_FILE/AP0C01055\\_SI\\_001.PDF](https://doi.org/10.1021/ACSAPM.0C01055/SUPPL_FILE/AP0C01055_SI_001.PDF).
- Williamson, G.K., Smallman, R.E., 1956. III. Dislocation densities in some annealed and cold-worked metals from measurements on the X-ray Debye-Scherrer spectrum. *Philosophical Magazine* 1, 34–46. <https://doi.org/10.1080/14786435608238074>.
- Wu, J.M., 2001. Nano-sized amorphous alumina particles obtained by ball milling ZnO and Al powder mixture. *Mater Lett* 48, 324–330. [https://doi.org/10.1016/S0167-577X\(00\)00321-9](https://doi.org/10.1016/S0167-577X(00)00321-9).
- Yacob, A.R., Bello, A.M., Kabo, K.S., 2016. The effect of polyoxyethylene (40) stearate surfactant on novel synthesis of mesoporous  $\gamma$ -alumina from Kano kaolin. *Arabian Journal of Chemistry* 9, 297–304. <https://doi.org/10.1016/j.arabjc.2015.06.039>.
- Yang, H., Liu, M., Ouyang, J., 2010. Novel synthesis and characterization of nanosized  $\gamma$ - $Al_2O_3$  from kaolin. *Appl Clay Sci* 47, 438–443. <https://doi.org/10.1016/j.clay.2009.12.021>.
- Yi, J. hong, Sun, Y. yi, Gao, J. feng, Xu, C. yan, 2009. Synthesis of crystalline  $\gamma$ - $Al_2O_3$  with high purity. *Transactions of Nonferrous Metals Society of China (English Edition)* 19, 1237–1242. [https://doi.org/10.1016/S1003-6326\(08\)60435-5](https://doi.org/10.1016/S1003-6326(08)60435-5).
- Zabeti, M., Wan Daud, W.M.A., Aroua, M.K., 2009. Activity of solid catalysts for biodiesel production: A review. *Fuel Processing Technology* 90, 770–777. <https://doi.org/10.1016/J.FUPROC.2009.03.010>.
- Zhang, H., Ruan, Y., Feng, Y., Su, M., Diao, Z., Chen, D., Hou, L., Lee, P.H., Shih, K., Kong, L., 2019. Solvent-free hydrothermal synthesis of gamma-aluminum oxide nanoparticles with selective adsorption of Congo red. *J Colloid Interface Sci* 536, 180–188. <https://doi.org/10.1016/j.jcis.2018.10.054>.
- Zhu, H.Y., Riches, J.D., Barry, J.C., 2002.  $\gamma$ -Alumina Nanofibers Prepared from Aluminum Hydrate with Poly(ethylene oxide) Surfactant. *Chemistry of Materials* 14, 2086–2093. <https://doi.org/10.1021/CM010736A>.